Eco-friendly facile synthesis of Co_3O_4–Pt nanorods for ethylene detection towards fruit quality monitoring

Dang Thi Thanh Le[1, *], Do Thi Ngoc Tram[2], Do Van Minh[1,2], Matteo Tonezzer[3,4], Tran Vu Diem Ngoc[5], Chu Thi Xuan[1], Chu Manh Hung[1], Nguyen Van Duy[1], Nguyen Duc Hoa[1, *]

[1]International Training Institute for Materials Science (ITIMS), Hanoi University of Science and Technology (HUST), No. 1, Dai Co Viet, Hanoi, Vietnam

[2]School of Engineering Physics (SEP), Hanoi University of Science and Technology (HUST), No. 1, Dai Co Viet, Hanoi, Vietnam

[3]Department of Chemical and Geological Sciences, University of Cagliari, Campus of Monserrato (CA), I-09042, Monserrato, Italy

[4]Center Agriculture Food Environment, University of Trento/Fondazione Edmund Mach, Via E. Mach 1, 38010, San Michele all'Adige, Italy

[5]School of Materials Science and Engineering (MSE), Hanoi University of Science and Technology (HUST), No. 1, Dai Co Viet, Hanoi, Vietnam

* Corresponding authors: thanhle@itims.edu.vn/le.dangthithanh@hust.edu.vn (DTT Le); ndhoa@itims.edu.vn/hoa.nguyenduc@hust.edu.vn (ND Hoa)

Abstract. Ethylene, a biomarker widely employed for evaluating fruit ripening during storage, exists at extremely low concentrations. Therefore a gas sensor with high sensitivity and a sub-ppm detection limit is needed. In this work, porous Co_3O_4 nanorods were synthesized through a hydrothermal method involving $Co(NO_3)_2$, $Na_2C_2O_4$, H_2O and ethylene glycol (EG), followed by annealing at 400 °C in air. The surface of the porous Co_3O_4 nanorods was functionalized with Pt nanoparticles to enhance the ethylene sensing performance. The effect of Co_3O_4 surface functionalisation with Pt nanoparticles was investigated by adding different amounts of nanoparticles. The sensor's outstanding performance at the optimum working temperature of 250 °C is attributed to the synergy between the high catalytic activity of Pt nanoparticles and the extensive surface area of the porous Co_3O_4 nanorods. Compared to pure Co_3O_4, the 0.031 wt% Pt sensor showed better ethylene sensing performance with a response 3.4 times that of pristine Co_3O_4. The device also demonstrated high selectivity, repeatability, long-term stability and a detection limit of 0.13 ppm for ethylene, which is adequate for fruit quality monitoring. The gas sensing mechanism of porous Co_3O_4 nanorods and the influence of Pt decoration on sensor performance are discussed.

Keywords: gas sensor; cobalt oxide; nanorods; ethylene detection; fruit quality monitoring.

1. Introduction

Ethylene, denoted by the chemical formula C_2H_4, is classified as the simplest alkene. It exists as a colorless and odorless gas and is naturally emitted by fruit during the ripening process [1]. Ethylene plays a crucial role in both fruit ripening and spoilage dynamics. Certain fruits, known as climacteric fruits, release ethylene, which subsequently accelerates the ripening process and ultimately leads to fruit decomposition. Monitoring the ethylene concentration during storage or inside the packaging allows for the estimation of fruit ripeness [2]. However, detecting ethylene poses challenges due to its small molecular size and low chemical reactivity [3]. Ethylene at a concentration as low as 1 part per million (ppm) is capable of initiating the ripening process in climacteric fruits [10.1016/j.tifs.2019.06.010]. Once the ripening process is triggered, the internal concentration of ethylene can quickly rise to saturation levels, and its reduction becomes difficult due to the significant diffusion resistance presented by the fruit's flesh and peel [10.1016/S0925-5214(98)00091-X]. Furthermore, the sensitivity of fruits to ethylene varies depending on the type of fruit. For example, Thap Maeo bananas require exposure to 10 ppm of ethylene to induce ripening [10.1016/j.foodres.2017.11.007], while prolonged exposure to 10 parts per billion (ppb) of ethylene in storage conditions can negatively impact the quality of mandarins [10.1016/j.foodchem.2017.09.088]. Even exposure to 10 ppb of ethylene from an external source can accelerate the softening process in kiwi fruits [10.1016/j.postharvbio.2011.09.011]. Hence, the development of highly sensitive sensors with low detection limit is crucial for effectively monitoring and controlling ethylene concentrations. Current methods for detecting ethylene include gas chromatography, laser acoustic spectroscopy, electrochemical sensors, electrocatalytic sensors, and non-dispersive infrared spectroscopy [4][5]. However, these techniques are not well-suited for field measurements due to their drawbacks, including high cost, time-consuming procedures, and the need for specialized personnel. In contrast, metal oxide gas chemosensors have garnered attention for

gas detection purposes, owing to their favorable attributes such as ease of production, compact size, cost-effectiveness, and seamless integration into electronic circuits [6]. Gas sensors offer valuable insights into the presence and concentration of specific gases, finding wide application in fields such as food quality assessment, hazardous gas monitoring, and industrial safety [7].

In recent times, there has been considerable research interest in p-type metal oxides due to their intriguing characteristics, including low susceptibility to moisture and good catalytic properties. These properties render p-type metal oxides promising candidates for developing high-performance gas sensors [8]. Cobalt oxide (Co_3O_4) is a wide bandgap (2.13 eV) p-type metal oxide semiconductor with spinel structure and face-centered cubic arrangement, suitable for gas detection of various gases such as ethanol [9], acetone [10], ammonia [11], formaldehyde [12] and triethylamine [13]. Several methods have been used for the growth of 1D Co_3O_4 nanostructures, such as electrospinning [14], sacrificial template [15], pulsed laser deposition [16], sputtering [17], and chemical vapor deposition [18]. Nevertheless, many deposition techniques utilized in gas sensor fabrication necessitate stringent parameters like high temperature or high vacuum conditions, resulting in costly processes that hinder the widespread adoption of these materials. In contrast, hydrothermal synthesis offers a simpler and more cost-effective alternative, allowing for adjustment of material shape and porosity [19]. However, the pristine Co_3O_4 material exhibits limited gas response, requiring surface functionalization with noble metal nanoparticles to enhance its performance. Notably, employing catalysts such as Pt, Ag, or Au on the facade of metal oxide semiconductor (MOS) is a common strategy to improve gas sensing capabilities [20,15,18]. However, it is worth mentioning that there have been relatively few publications to date on the synthesis of Co_3O_4 nanostructures with surface decoration specifically for ethylene detection.

This study introduces a novel, ecological, and surfactant-free approach for the growth of porous Co_3O_4 nanorods and the development of a gas sensor tailored for the detection of ethylene gas

in agro-food applications. The proposed method offers the advantage of scalable synthesis of Co_3O_4 nanorods with tunable porosity, enabling enhanced surface exposure for efficient gas adsorption. The authors have previously reported the synthesis of cobalt oxide nanorods using this technique in a conference paper [21]. To further ameliorate the gas sensing performance, the surface of the porous Co_3O_4 nanorods was decorated with Pt nanoparticles, leveraging the synergistic effects arising from the high catalytic activity and the Co_3O_4–Pt heterojunction. The resulting sensors exhibit excellent response, capable of detecting ethylene gas at sub-ppm concentrations, meeting the practical requirements for fruit ripening assessment.

2. Experimental

2.1. Synthesis of Co_3O_4 porous nanorods

Cobalt nitrate, ethylene glycol (EG), and sodium oxalate obtained from Sigma-Aldrich, all of analytical grade, were used without further purification. The synthesis of Co_3O_4 nanorods was achieved via a straightforward and ecological hydrothermal method, as illustrated in Fig. 1. In a typical synthesis, a solution was prepared by dissolving 0.016 moles of cobalt(II) nitrate hexahydrate ($Co(NO_3)_2 \cdot 6H_2O$) and 0.009 moles of sodium oxalate ($Na_2C_2O_4$) in a mixture of 50 mL deionized water and ethylene glycol. The ratio of water to ethylene glycol was 1:2. This resulted in the formation of a pinkish transparent solution. The prepared solution was then transferred to a 100 mL teflon-lined stainless-steel autoclave. The autoclave was placed in an electric oven and maintained at a temperature of 200 °C for a duration of 24 hours. After the heating period, the autoclave was allowed to cool down to room temperature. The resulting precipitate was separated from the solution by centrifugation. To eliminate impurity ions, the collected precipitate was washed multiple times using ethanol and deionized water. Following the washing process, the precipitate was carefully dried at a temperature of 80 °C for a duration of 24 hours. Subsequently, the dried precipitate underwent annealing in the presence of air, at

a temperature of 400 °C for a duration of 2 hours.

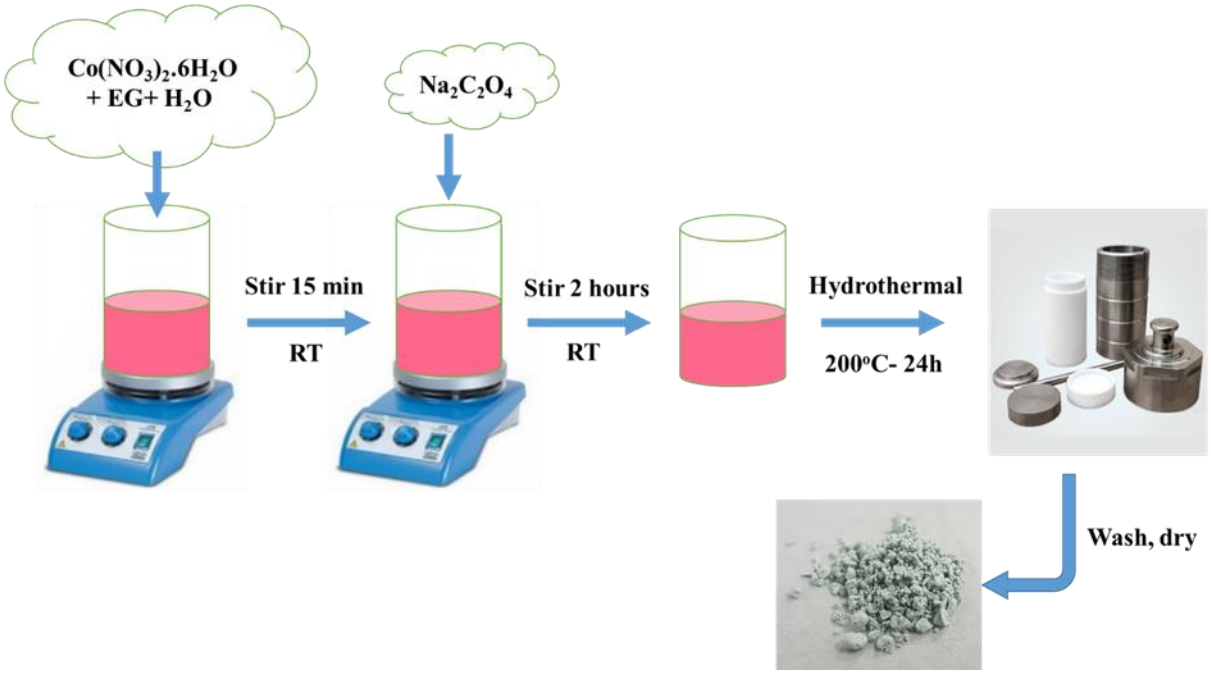

Fig. 1. The synthesis procedure of cobalt oxalate hydrate nanorods.

2.2. Fabrication of Pt–Co_3O_4 nanorods sensors

The surface of Co_3O_4 nanorods was modified by adding ultrafine Pt nanoparticles with a diameter ranging from 3 to 5 nm. The synthesis method for these Pt nanoparticles is extensively described in reference [22], utilizing a modified polyol method outlined in reference [23]. In a typical procedure, a colloidal solution containing Pt nanoparticles was added to a mixture comprising 10 mg of hydrothermal product ($C_2CoO_4 \cdot 2H_2O$) and 2 mL of N-vinylpyrrolidone (NVP). Ultrasonication was then performed for 10 seconds to achieve a homogeneous colloidal solution. Four sets of gas sensors were fabricated using the drop-casting technique described in reference [24], employing different quantities of Pt nanoparticles. The Pt contents in these samples were 0, 0.026, 0.031, and 0.038 weight percent (wt.%), respectively. The corresponding sensors were denoted as Co–Pt0, Co–Pt1, Co–Pt2, and Co–Pt3. Once applied onto the substrate, each material was dried at 120 °C for 1 hour, followed by calcination at 400 °C for 2 hours with a rate of 2 °C/min to form a thick film sensor.

2.3. Materials and sensors characterizations

The crystallographic structure of the Co_3O_4 nanomaterials was characterized using X-ray diffraction (XRD) analysis conducted on a Bruker-D8 Advance instrument. CuKα radiation with a wavelength of 0.15406 nm was employed. The morphology of the nanostructures was examined through scanning electron microscopy (SEM) using a Hitachi S-4700 instrument with an accelerating voltage of 5 kV. The microstructure of the nanomaterials was further investigated using high-resolution transmission electron microscopy (HRTEM) coupled with selected area electron diffraction (SAED). The HRTEM and SAED measurements were performed at an accelerating voltage of 200 kV using a JEOL 2100F instrument. The sensing properties of the Co_3O_4–Pt sensors were evaluated using a custom-built experimental setup [25]. Prior to conducting the measurements, each sensor underwent a preheating process at 400 °C for a duration of 2 hours. This was done to ensure the stability of the resistance and enhance the contact between the Pt electrodes and the cobalt oxide. The sensor resistance was monitored using a source meter (Keithley 2602) while introducing the target gas into the measurement chamber and subsequently evacuating it. The sensor's response (S) was determined by calculating the ratio of R_g/R_a for reducing gases or R_a/R_g for oxidizing gases. In this context, R_a represents the resistance of the sensor in ambient air, while R_g corresponds to the resistance of the sensor when exposed to the specific gas being analyzed. The response time (τ_{resp}) and recovery time (τ_{recov}) were determined by measuring the time required for the sensor's response to reach 90% saturation after exposure to the analyte gas and air, respectively.

3. Results and Discussion

3.1. Morphological, compositional and structural characterization

The nanorods obtained after hydrothermal growth exhibited a smooth morphology with a

diameter ranging from 200 to 500 nm and a length from 5 to 20 µm. SEM images of the hydrothermally synthesized nanorods are presented in Fig. 2(A, B), revealing straight nanorods with uniform diameters and smooth surfaces. The aspect ratio, defined as the ratio between the diameter and length of the nanorods, depends on the temperature and duration of the hydrothermal process. After subjecting the cobalt oxalate hydrate nanorods to calcination at 400 °C for 2 hours, a noticeable change in their morphology was observed. The nanorods transformed into porous nanostructures, as depicted in Fig. 2(C, D). The resulting Co_3O_4 nanorods were composed of spherical nanoparticles with diameters ranging from 10 to 30 nm.

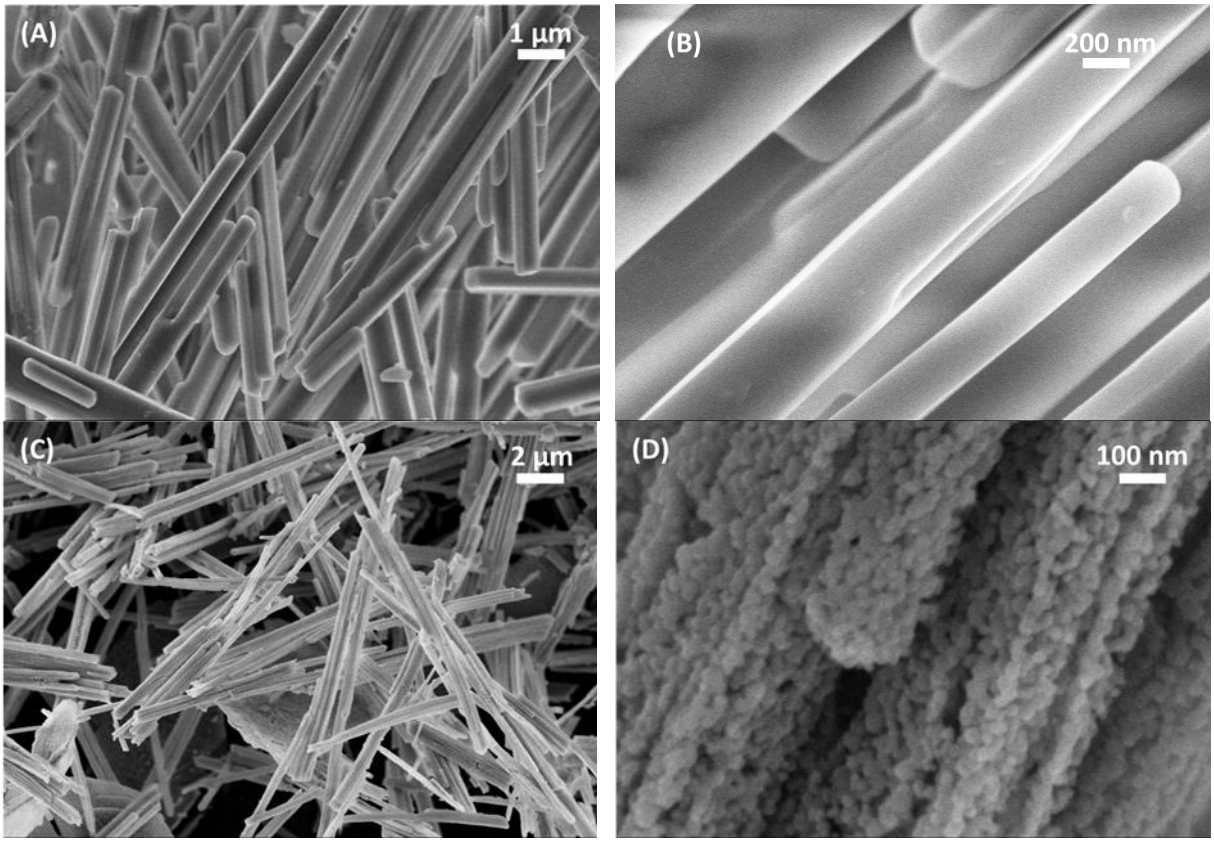

Fig. 2. FESEM images of the cobalt oxide nanorods at diverse magnifications before (A, B) and after heat treatment (sample Co–Pt0) (C, D).

The elemental composition of the samples prior to thermal treatment was examined using energy-dispersive X-ray spectroscopy. The corresponding spectrum, obtained from the

analyzed region shown in Fig. 3(A), is presented in Fig. 3(B). The spectrum reveals characteristic peaks associated with carbon, cobalt, and oxygen. Moreover, elemental mapping of the nanomaterial, as depicted in Figures 3(C, D, E), illustrates the uniform distribution of cobalt (in red), oxygen (in green), and carbon (in cyan) throughout the analyzed area.

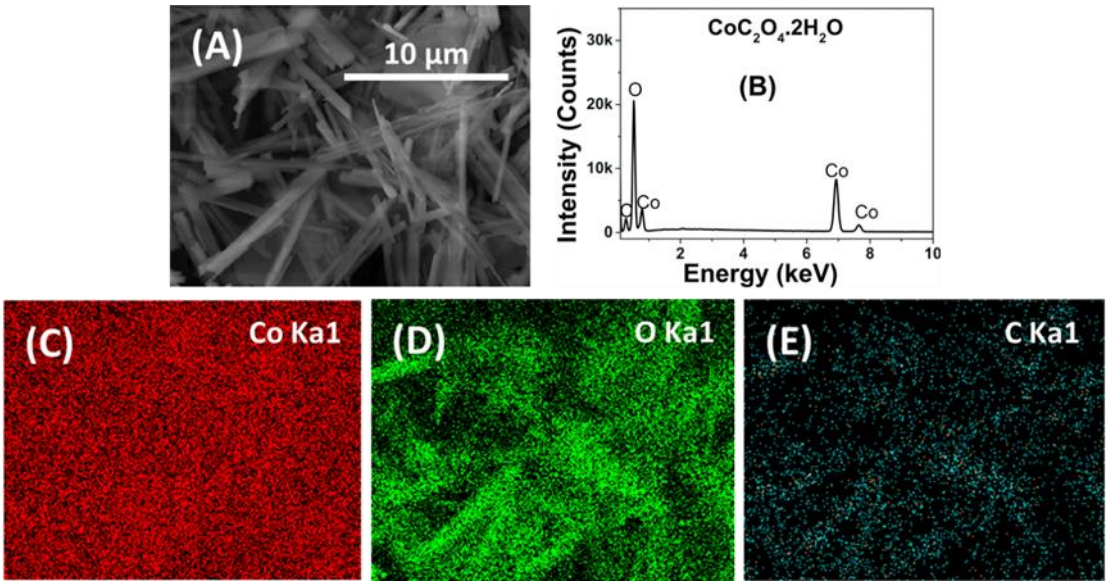

Fig. 3. SEM image (A), EDX spectrum (B) and elemental maps of as-prepared cobalt oxalate hydrate nanorods: Co (C), O (D), and C (E).

The crystal structure and phase of the nanorods were examined using XRD analysis after the hydrothermal growth and subsequent annealing processes. The corresponding XRD patterns are presented in Fig. 4(A, B). The XRD pattern of the nanorods obtained through hydrothermal growth exhibited characteristic peaks consistent with the monoclinic phase of cobalt oxalate (α- $C_2CoO_4 \cdot 2H_2O$), as identified by the JCPDS No. 025–0251. Notably, the main peaks could be attributed to the (-202), (200), (002), and (-402) crystallographic planes (Fig. 4(A)). After the calcination at 400 °C for a duration of 2 hours, a phase transformation from the monoclinic cobalt oxalate to the cubic phase of Co_3O_4 was observed in the nanorods (Fig. 4(B)). The main peaks in the XRD pattern corresponded to the (220), (311), (400), (511), and (440) crystallographic planes of the face-centered cubic phase of Co_3O_4, as indicated by the JCPDS

No. 042−1467. Importantly, no discernible peaks originating from impurities or other phases were detected, indicating the successful formation of a single-phase Co_3O_4 material. Only one XRD pattern of Co_3O_4 after annealing is shown since the patterns of the four samples are identical. In fact, the amount of Pt is too low for it to be appreciable for the instrument.

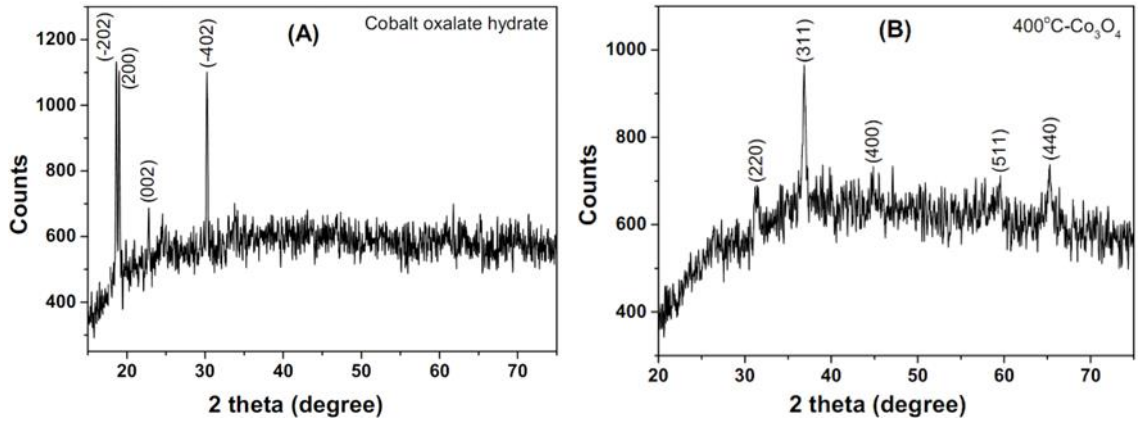

Fig. 4. XRD patterns of nanorods (a) before and (b) after the heat treatment at 400 °C (sample Co–Pt0).

Three samples, namely Co–Pt1, Co–Pt2, and Co–Pt3, were prepared with varying amounts of Pt. Subsequently, during the characterization process, particular attention was given to the sample labeled Co–Pt2 due to its highest sensing performance. The annealed Co_3O_4 nanorods from Co–Pt2 sample were characterized by EDX and elemental mapping, as shown in Fig. 5. The EDX spectrum of Co–Pt2 in Fig. 5(B) clearly shows the presence of Co, O, and Pt in the nanorods of Fig. 5(A). The elemental maps in Fig. 5(C, D, E) demonstrate that the dispersion of Co, O, and Pt elements is homogeneous in the nanomaterial. Although Pt nanoparticles are difficult to see due to their tiny size, the appearance of Pt peaks in the pattern in Fig. 5(B) and the homogeneous presence of the element in the elemental map in Fig. 5(E) demonstrate that the Pt nanoparticles were successfully distributed on the facade of the Co_3O_4 nanorods.

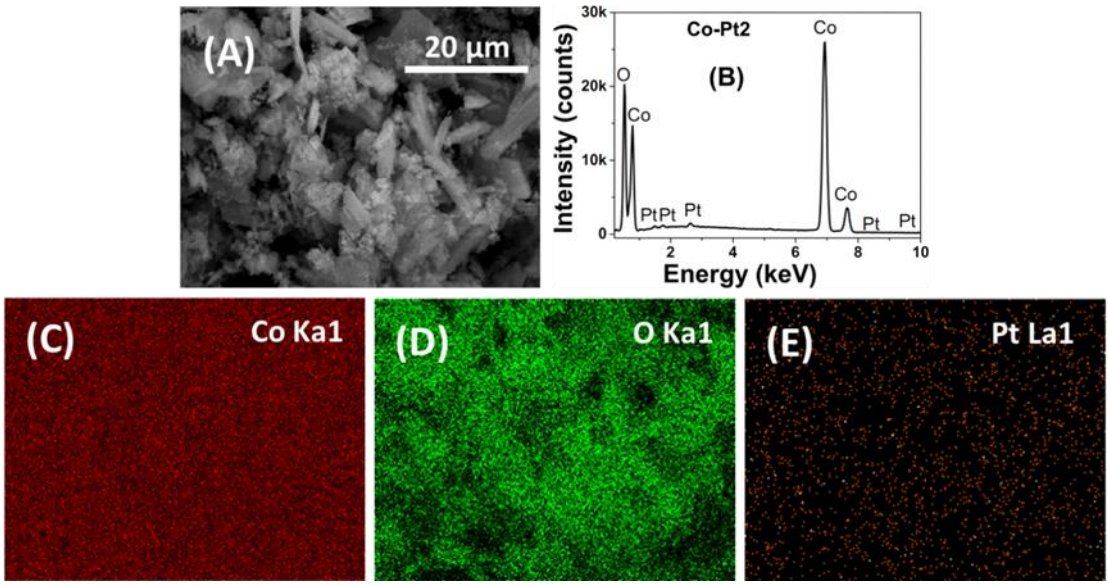

Fig. 5. SEM image (A), EDX spectrum (B) and elemental maps of Co–Pt2 nanorods after the heat treatment at 400 °C: Co (C), O (D), and Pt (E).

Figure 6 illustrates TEM, HRTEM, and SAED images of different nanorods: cobalt oxalate hydrate nanorods prior to thermal annealing, cobalt oxide porous nanorods after annealing, and Co_3O_4–Pt nanorods following surface decoration. The cobalt oxalate dihydrate nanorods (Fig. 6(A)) exhibit a smooth and rounded surface. The SAED pattern obtained from the corresponding $C_2CoO_4 \cdot 2H_2O$ nanorod (inset of Fig. 6(A)) displays continuous rings indicative of its amorphous structure. However, the HRTEM image (Fig. 6(B)) reveals slight indications of lattice fringes, although they are of limited length and not particularly well-defined. This observation suggests that the $C_2CoO_4 \cdot 2H_2O$ nanorods are characterized by a limited degree of crystallization.

Following annealing, the cobalt oxalate nanorods retain their size but undergo dehydration, resulting in the formation of porous Co_3O_4 nanorods (Fig. 6(C)). These nanorods consist of interconnected nanograins with significant void spaces between them. The porous structure enhances the surface area and facilitates gas transport, thereby contributing to improved gas sensing properties. The corresponding SAED image (inset in Fig. 6(C)) exhibits bright dot

rings, indicating high crystallinity of the polycrystalline Co_3O_4 nanorod grains. This finding is in agreement with the HRTEM image (Fig. 6(D)), where clear lattice fringes corresponding to the (111) and (311) crystal planes show good crystallinity. The SAED image of the Co–Pt2 sample (Fig. 6(E)) showcases a well-defined and systematic diffraction pattern, affirming the crystalline nature of the cobalt oxide nanorods. The main diffraction points correspond to the (400), (311), (220), (333), and (440) crystallographic planes of Co_3O_4. Furthermore, the HRTEM image of the Co–Pt2 sample (Fig. 6(F)) reveals the interconnected presence of platinum (Pt) nanoparticles with cobalt oxide nanograins. The Pt nanoparticles appear as dark spots in the HRTEM image due to their higher density. This result underlines the successful functionalization of the Co_3O_4 nanorods surface with finely dispersed Pt nanoparticles.

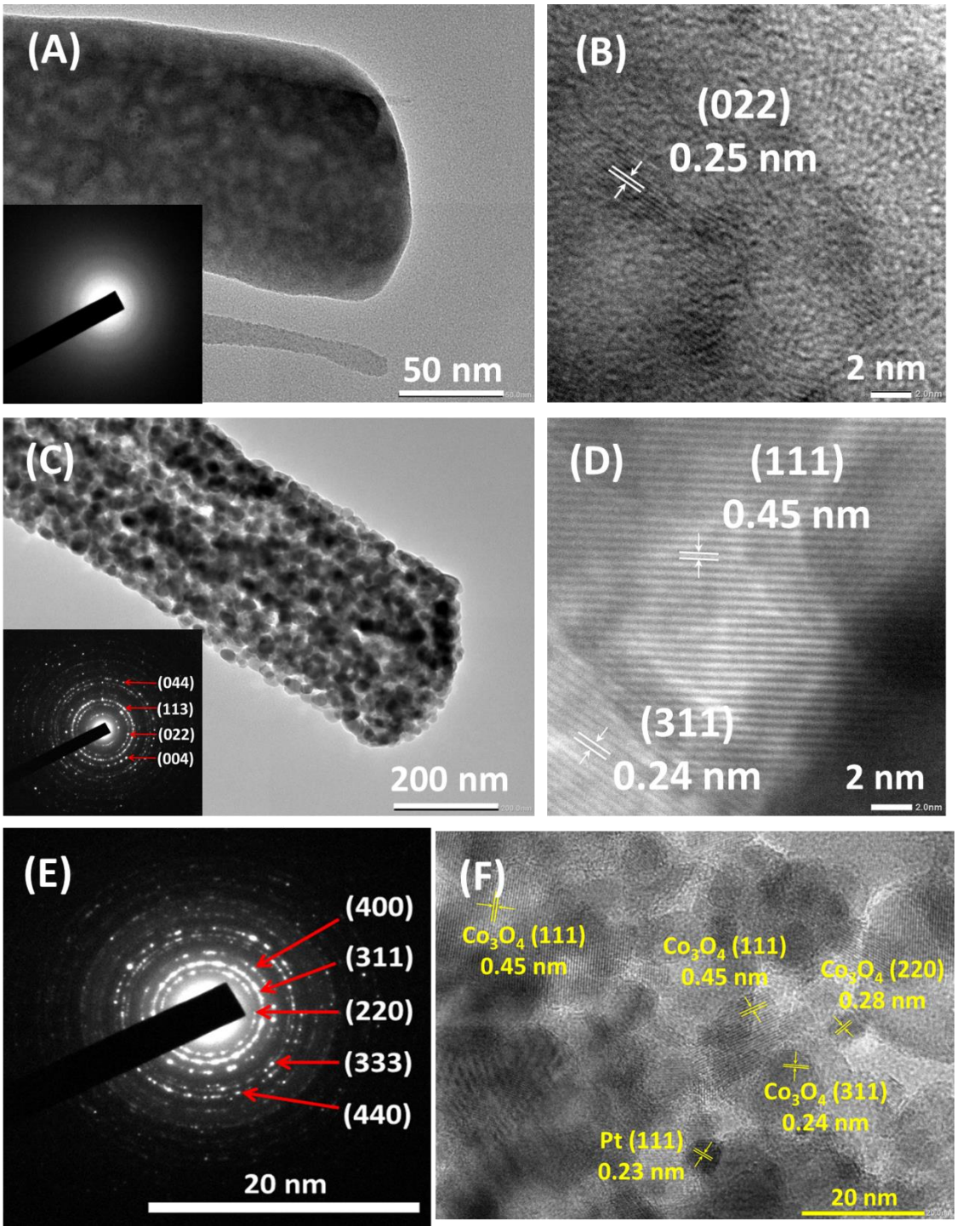

Fig. 6. TEM and HRTEM images of (A, B) cobalt oxalate dihydrate nanorods, (C,D) Co_3O_4 polycrystalline nanorods (sample Co–Pt0), (E) SAED image of Co_3O_4 polycrystalline nanorods and (F) HRTEM of Co_3O_4–Pt nanorods from sample Co–Pt2. The insets in (A,C) show the SAED patterns from the two respective materials.

Probable formation mechanism of $CoC_2O_4{\cdot}2H_2O$ and Co_3O_4 nanorods

During the hydrothermal process, the compound $Co(NO_3)_2$ undergoes a reaction with $Na_2C_2O_4$ and H_2O, resulting in the formation of $CoC_2O_4{\cdot}2H_2O$ nanorods. Subsequently, when these nanorods are subjected to heating in air, they undergo a decomposition process. Initially, the nanorods decompose into CoC_2O_4 and H_2O. Following this, the water (H_2O) evaporates, leaving behind CoC_2O_4. Subsequently, the CoC_2O_4 reacts with O_2, leading to the formation of Co_3O_4 and CO_2. This hypothesis agrees with the chemical reactions outlined in reference [26]:

$$Co(NO_3)_2 + Na_2C_2O_4 + 2H_2O \leftrightarrow CoC_2O_4{\cdot}2H_2O + 2NaNO_3 \quad (1)$$

$$CoC_2O_4{\cdot}2H_2O \leftrightarrow CoC_2O_4 + 2H_2O \quad (2)$$

$$3CoC_2O_4 + 2O_2 \leftrightarrow Co_3O_4 + 6CO_2 \quad (3)$$

The evaporation of H_2O and CO_2, as described in equations (2) and (3), contributes to weight loss. This weight loss is responsible for the formation of pores between the nanograins, increasing the porosity of the Co_3O_4 nanorods. These findings are in accordance with the scientific literature [19] and the SEM and TEM images.

3.2. Electrical and gas sensing characteristic of Co_3O_4 nanorods-based sensor

The electrical characteristics of the Co–Pt0 and Co–Pt2 sensors were compared by analyzing the current-voltage (*I–V*) curves at various temperatures in air. Both sensors exhibited a predominantly linear behavior, indicating the presence of an ohmic contact between the sensing material and the metal electrodes (Fig. 7(A, B)). This observation is in line with expectations, as the work function of Co_3O_4 is approximately 4.5 eV [27]. This value is lower than the work function of Pt, which is approximately 5.35 eV. Consequently, an ohmic contact is established at the boundary between the Pt electrode and the Co_3O_4 sensing nanomaterial. The presence of an ohmic contact is crucial for ensuring stable and consistent performance of the sensors [28]. Furthermore, both devices exhibited an increase in current with rising temperature.

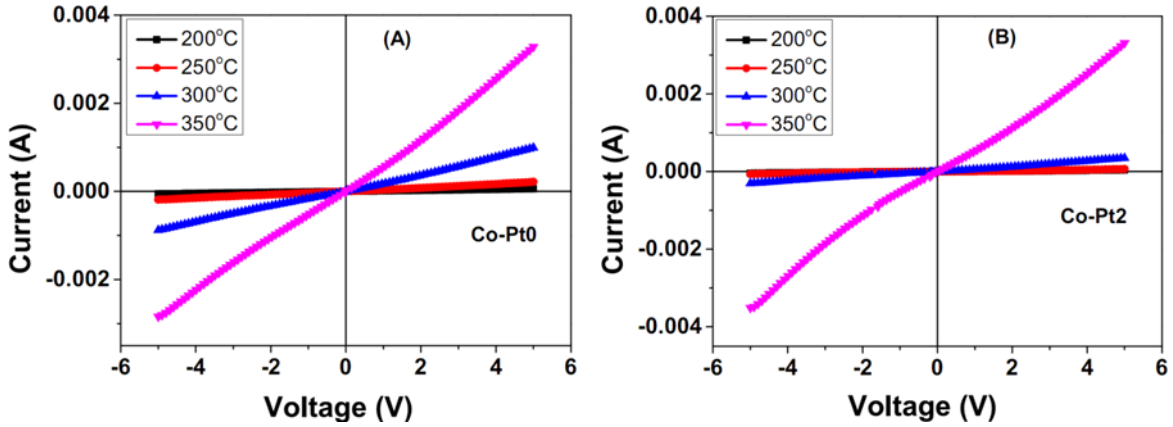

Fig. 7. *I–V* plots of Co–Pt0 (A), and Co–Pt2 (B) sensors recorded at diverse temperatures.

The performance of the Co–Pt0, Co–Pt1, Co–Pt2, and Co–Pt3 sensors towards different concentrations of ethylene (ranging from 10 to 500 ppm) at various temperatures (ranging from 200 to 350 °C) was evaluated and presented in four radar plots in Fig. 8(A-D). The pure Co_3O_4 sensor (Co–Pt0, Fig. 8(A)) exhibited a consistent response across different temperatures, which increased with the concentration of ethylene, particularly at 500 ppm. At 250 °C, it displayed a maximum response of 1.32 (please note the difference in scale in Fig. 8(A) compared to (B-D)). The Co–Pt1 sensor (Fig. 8(B)) demonstrated an optimal working temperature of 250 °C, exhibiting significantly higher response compared to other temperatures, with a maximum value of 4.5 per 500 ppm of ethylene. This represented a 3.4-fold increase in response compared to pure Co_3O_4, attributed to the presence of Pt nanoparticles on the surface of the nanowires. Similarly, the Co–Pt2 sensor (Fig. 8(C)) exhibited an improved response at 200 °C but displayed its maximum response at 250 °C, reaching a value of 4.3 for 500 ppm ethylene. The Co–Pt3 sensor also demonstrated its best working temperature at 250 °C, as depicted in Fig. 8(D). The maximum response to 500 ppm of ethylene at 250 °C was slightly lower, with a value of 3.6. These findings indicate that increasing the amount of Pt nanoparticles on the Co_3O_4 surface up to 0.031 wt% enhances sensor performance, but beyond this threshold, the response decreases. The responses of the four Co–Pt sensors to different ethylene concentrations at 250

°C are displayed in Fig. 8(E) using distinct colors. The Co–Pt2 sensor demonstrated the highest response at low concentrations (≤100 ppm), while the Co–Pt1 sensor exhibited the highest response at 500 ppm. Based on these findings, the Co–Pt2 sensor was selected for further characterizations and analyses in this study. Figure 8(F) provides a comparison of the sensor responses at different temperatures for 50 ppm ethylene. Notably, all sensors exhibited their maximum response at a temperature of 250 °C, which was consequently chosen as the working temperature for subsequent analyses.

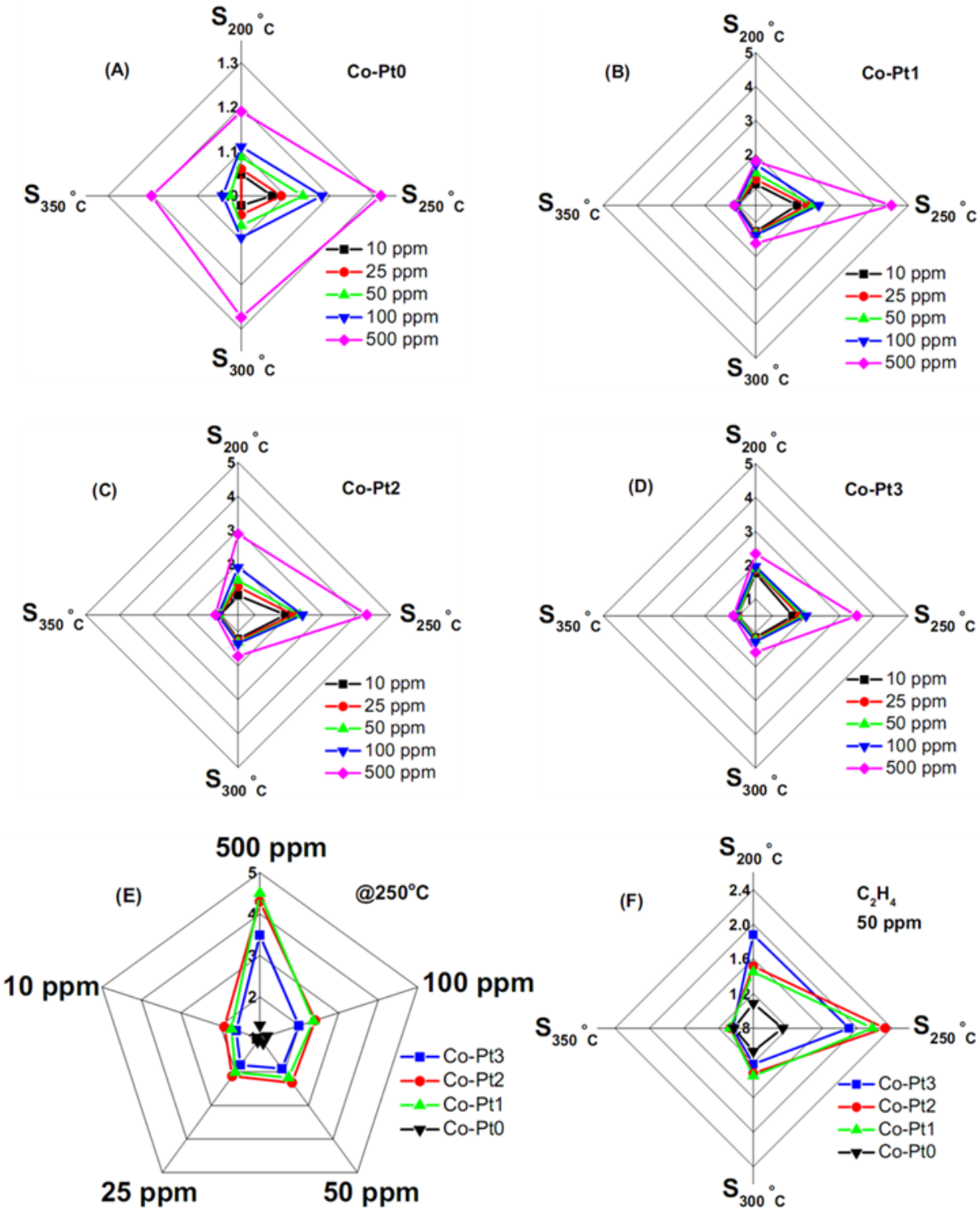

Fig. 8. Radar plots displayed ethylene response of the Co–Pt sensors: (A) Co–Pt0; (B) Co–Pt1; (C) Co–Pt2; (D) Co–Pt3. (E) Response to 50 ppm ethylene of the four sensors as a function of temperature; (F) Response at 250 °C of the four sensors as a function of ethylene concentration.

The response values of the four sensors measured at 250 °C are depicted in the radar plot presented in Fig. 9(A). The response plots for various ethylene concentrations exhibit a similar shape, highlighting that the pure Co_3O_4 sensor (Co–Pt0) demonstrates a notably low response compared to the others. At high concentrations, the Co–Pt1 sensor exhibits the highest response, closely followed by the Co–Pt2 sensor, while at low concentrations it is the opposite. Figure 9(B) displays the radar plots illustrating the response of the Co–Pt2 sensor at different working temperatures and various ethylene concentrations. Notably, the minimum response is observed at 350 °C, while the maximum response occurs at 250 °C.

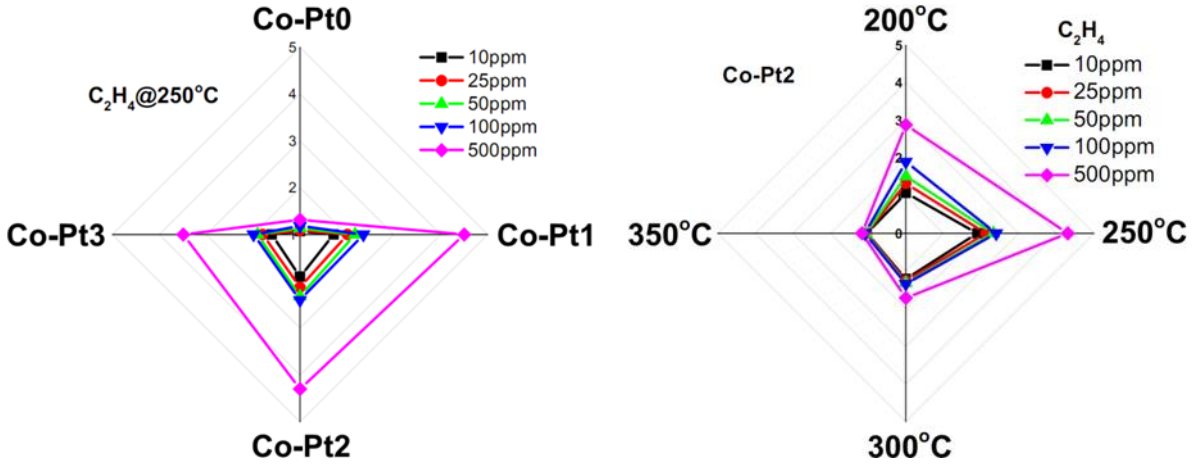

Fig. 9. Radar plots about the response of the sensors Co–Pt0, Co–Pt1, Co–Pt2 and Co–Pt3 to different concentrations of ethylene at 250 °C (A), and the response of the Co–Pt2 sensor at diverse working temperatures to several concentrations of ethylene gas.

Gas sensing mechanism

The gas-sensing mechanism of Co_3O_4 materials relies on chemical interactions between gaseous molecules, particularly oxygen and the desired gas, at the surface of the metal oxide [29]. Upon exposure of Co_3O_4 to air, oxygen molecules are adsorbed onto its facade, capturing electrons from the conduction band of Co_3O_4 and leading to the generation of oxygen ions. The formation of oxygen ions is temperature-dependent and occurs according to the following reactions, which are influenced by the working temperature [29][30]:

$$O_{2\ gas} \leftrightarrow O_{2\ ads} \quad (4)$$

$$O_{2\ ads} + e^{-} \leftrightarrow O_2^{-}{}_{ads},\ T < 150\ °C \quad (5)$$

$$O_{2\ ads} + 2e^{-} \leftrightarrow 2O^{-}{}_{ads},\ 150\ °C \leq T \leq 350\ °C \quad (6)$$

$$O^{-}{}_{ads} + e^{-} \leftrightarrow O^{2-}{}_{ads},\ T > 350\ °C \quad (7)$$

These responses result in the creation of a layer with accumulated holes on the facade of the porous Co_3O_4 polycrystalline nanorods and this layer reduces the resistance of the sensor. Upon the interaction of the sensor with ethylene, the molecules of ethylene engage in chemical interactions with the absorbed oxygen ions. This interaction facilitates the liberation of electrons from the conduction band of Co_3O_4. These reactions can be written as [31,32]:

$$C_2H_{4\ ads} + 6O^{-}{}_{ads} \leftrightarrow 2CO_{2\ gas} + 2H_2O_{\ gas} + 6e^{-} \quad (8)$$

$$C_2H_{4\ ads} + 6O^{2-}{}_{ads} \leftrightarrow 2CO_{2\ gas} + 2H_2O_{\ gas} + 12e^{-} \quad (9)$$

$$e^{-} + h^{\circ} \leftrightarrow \text{Null} \quad (10)$$

The liberated electrons undergo recombination with the existing holes, leading to an elevation in the resistance of the sensor.

The gas-sensing mechanism proposed for the Co_3O_4–Pt functionalized sensors is depicted in Fig. 10. The enhanced response observed in sensors functionalized with Pt nanoparticles can be attributed to two distinct effects:

(1) Spillover during oxygen adsorption: When oxygen is adsorbed, the high catalytic activity of Pt nanoparticles facilitates the transfer of oxygen ions onto the Co_3O_4 surface, resulting in an increased number of chemisorbed oxygen ions. This, in turn, leads to the thickening of the hole accumulation layer formed at the interface between the Pt nanoparticles and the Co_3O_4 porous nanorods. (Refer to Fig. 10(A)).

(2) Creation of a hole accumulation layer: The presence of Pt nanoparticles on the surface of Co_3O_4 promotes the creation of a hole accumulation layer at the Pt–Co_3O_4 boundary. The accumulation of holes within this layer induces a bending of the energy bands at the interface

between Co_3O_4 and Pt. (Refer to Fig. 10(B)).

These effects together contribute to the enhanced gas-sensing properties observed in the Co_3O_4–Pt functionalized sensors. The proposed mechanism is supported by previous studies [33][34].

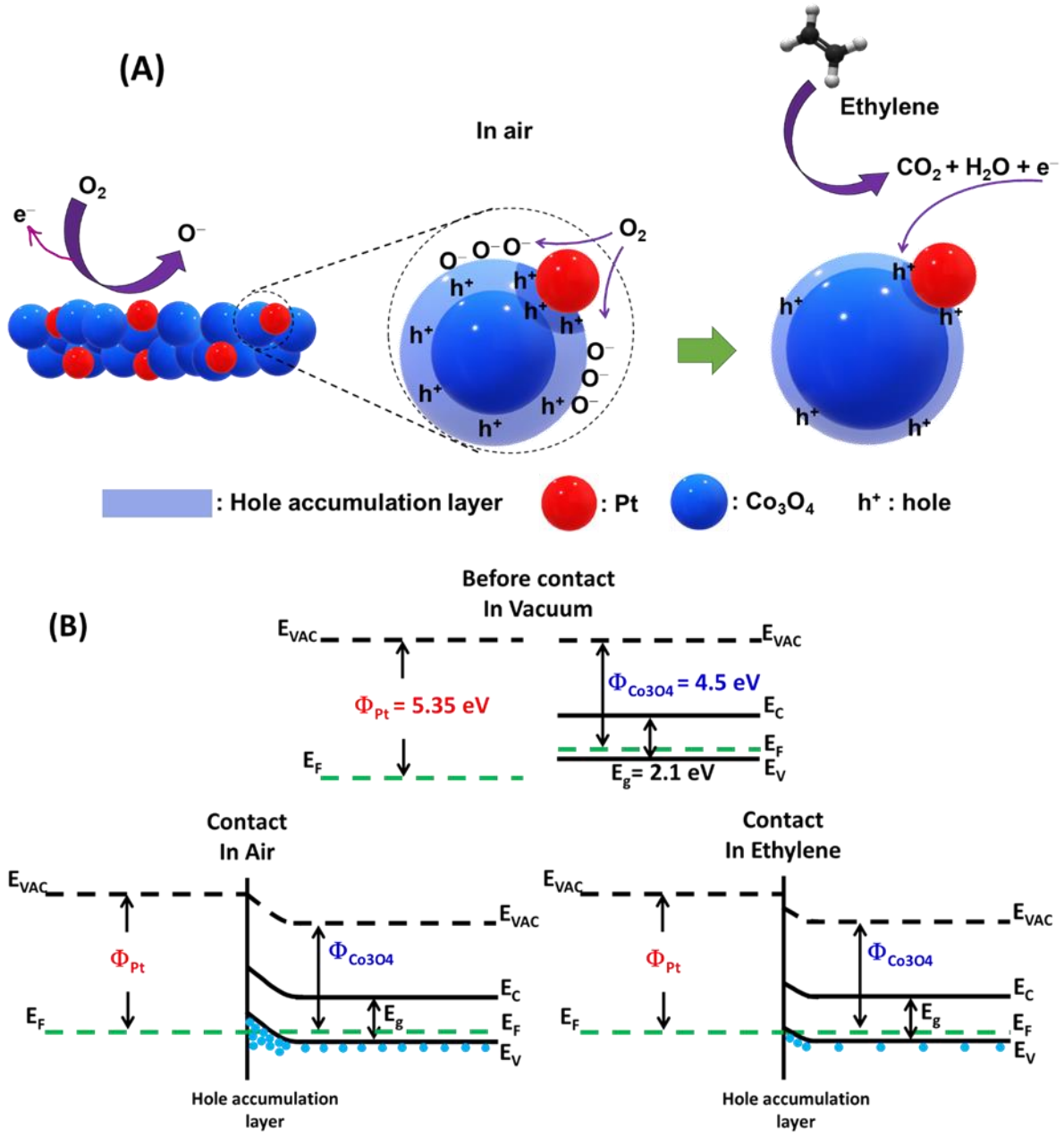

Fig. 10. (A) A propounded mechanism of ethylene sensing and (B) band diagram of the Co–Pt porous nanorods sensor.

The incorporation of Pt nanoparticles in Co_3O_4 materials results in the spillover effect, which generates additional reactive sites on the surface of the material. These reactive sites facilitate

the enhanced adsorption of oxygen ions, thereby increasing the availability of oxygen ions for subsequent reactions with ethylene molecules. Consequently, when the Co_3O_4–Pt sensor is exposed to ethylene, a larger number of ethylene molecules can react with the pre-absorbed oxygen ions, leading to a notable increase in resistance during ethylene detection. Furthermore, the presence of Pt nanoparticles introduces a higher work function (5.35 eV) compared to the p-type semiconductor Co_3O_4 (4.5 eV). This difference in work function enables electron transport through the interface from Co_3O_4 to Pt, thereby expanding the hole accumulation layer. The hole accumulation layer is particularly sensitive to changes in the surrounding environment, further augmenting the sensor response to ethylene [33]. With an increase in the amount of Pt, there is a corresponding increase in the formation of heterojunctions between Co_3O_4 and Pt, and an increased availability of oxygen ions via the spillover effect. These factors, in turn, contribute to the improved performance of the gas sensors. However, it should be noted that when the Pt content continues to increase, it can potentially hinder the reactions between oxygen ions and the target gas. This hindrance is attributed to the saturation of catalytic sensitization and catalyst aggregation, thereby causing a decrease in performance. These results align with the references [35],[36].

Figure 11(A) illustrates the dynamic resistance of the Co–Pt2 sensor when exposed to pulses of varying ethylene concentrations at the optimized working temperature of 250 °C. The sensor demonstrates excellent sensitivity and responsiveness, enabling the sharp detection of even small amounts of ethylene. Additionally, the sensor exhibits good recovery properties following exposure to ethylene. To determine the limit of detection for ethylene, a calculation was performed using three times the standard deviation of the signal in air and the sensitivity close to the origin. The obtained limit of detection was found to be 0.13 ppm. This sub-parts-per-million value is considered adequate for numerous practical applications, including food quality monitoring [2]. The response values obtained from Fig. 11(A) are further plotted in Fig. 11(B),

presenting the relationship between the response of the Co–Pt2 sensor and the concentration of ethylene.

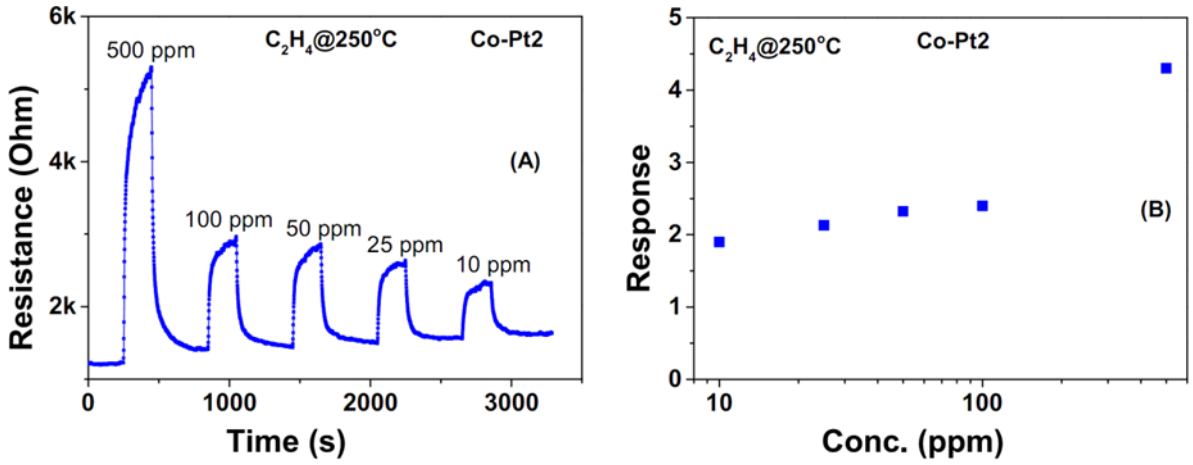

Fig. 11. The response of the Co–Pt2 sensor at 250 °C to different ethylene concentrations: (A) dynamic resistance to pulses of different ethylene concentrations; (B) response as a function of ethylene concentration.

Figure 12 extensively illustrates the behavior of the Co–Pt2 sensor as regards the working temperature and ethylene concentration. In Figure 12(A), the dynamic resistance of the sensor during exposure to different ethylene concentrations at four distinct working temperatures (200, 250, 300, and 350 °C) is presented. The corresponding response values derived from the dynamic resistance measurements are displayed in Figure 12(B). The sensor response increases with increasing ethylene concentration from 10 ppm to 500 ppm at all temperatures. This can be attributed to the higher number of ethylene molecules adsorbed on the nanomaterial surface, leading to an expansion of the hole accumulation layer. Furthermore, the response shows an increase as the working temperature rises from 200 to 250 °C, while beyond that the response tends to decrease. These results indicate that the introduction of Pt nanoparticles on the cobalt oxide surface effectively lowers the working temperature of the Co–Pt2 sensor. Figure 12(C) illustrates the response and recovery times as a function of the ethylene concentration, while Fig. 12(D) shows them as a function of the working temperature. At 250 °C, the response time

increases from 86 s (for 10 ppm) to 115 s (for 500 ppm), while the recovery time decreases from 103 s to 74 s for the same concentrations. These findings provide valuable insights into the sensor performance characteristics and highlight the dependence of response and recovery times on ethylene concentration and working temperature. The observed increase in response time with higher gas concentrations can be attributed to the greater number of ethylene molecules present, which leads to a higher saturation of active sites on the Co–Pt2 sensor's surface. As a result, the dynamic adsorption process takes more time to reach equilibrium. The experimental data suggests that the Co–Pt2 sensor exhibits extended recovery times at low gas concentrations but experiences a marked reduction in these times at high gas concentrations. The response times drastically decrease with increasing temperature (Fig. 12(D)) thanks to thermal energy which accelerates the reaction between ethylene molecules and the pre-adsorbed oxygen ions and also the desorption of ethylene molecules [22]. The recovery time also exhibits a significant decrease as the working temperature increases, which is consistent with the findings reported in reference [37]. Both the response time and the recovery time at the working temperature of 250 ^{o}C are less than two minutes, which is adequate for realistic applications in fruit quality monitoring.

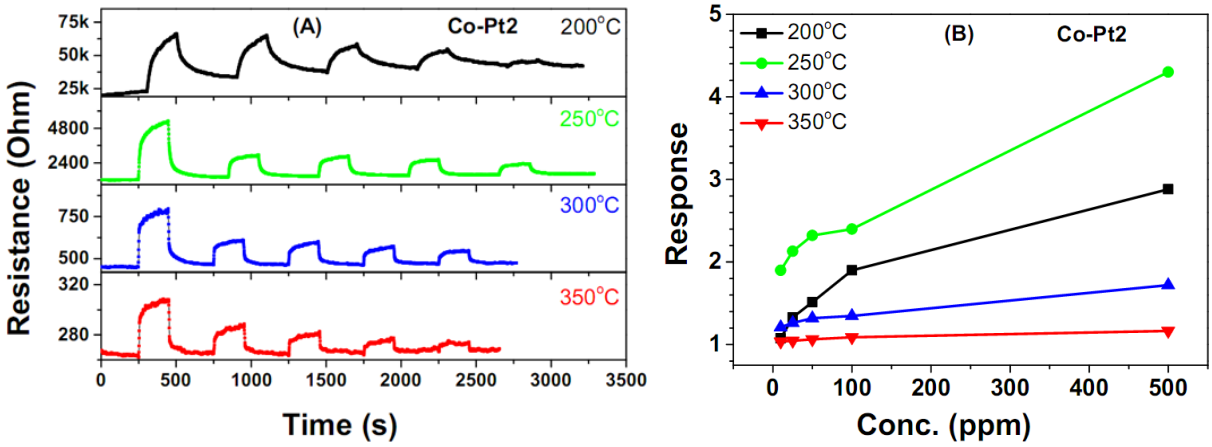

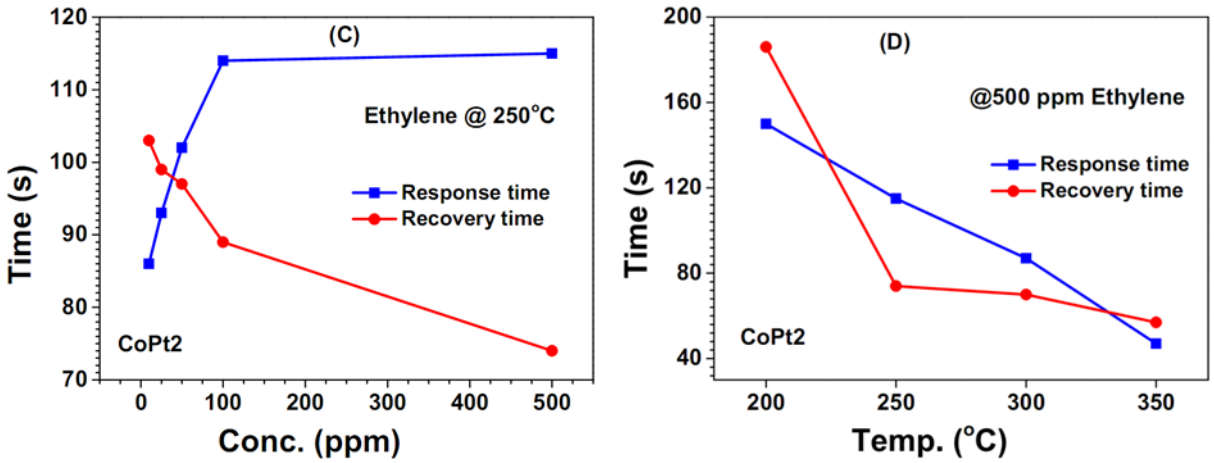

Fig. 12. (A) Dynamic resistance of the Co–Pt2 sensor at different temperatures (200–350 °C), (B) Sensor response as a function of ethylene gas concentration at various working temperatures, (C) response time and recovery time as a function of ethylene concentration, and (D) as a function of sensor working temperature.

Table 1 presents a concise overview of recent scientific literature on ethylene gas sensors, encompassing both n-type and p-type metal oxides. It shows that the Co–Pt2 sensor exhibits significantly higher response values to ethylene compared to several previously reported sensors. Notably, the Co–Pt2 sensor demonstrates a response 12.2 times greater than the MnO_2-Au sensor developed by Bigiani et al. [38], and 12.4 times higher than the TiO_2-5%WO_3 sensor created by Kathirvelan et al. [39]. It is worth highlighting that TiO_2 and WO_3 are n-type metal oxides, which generally exhibit superior gas sensing capabilities compared to p-type metal oxides. Moreover, when compared to similar materials, such as $LaFeO_3$ functionalized with Ag, the Co–Pt2 sensor showcases an exceptional ethylene-sensing performance with a response value 178.5 times higher [32].

Table 1. *Comparison of C_2H_4 detection performance of various materials in recent literature*.

Material	**Method**	**T (ºC)**	**Ethylene conc. (ppm)**	**Response**	**Limit of detection**	**Ref. (Year)**

					(ppm)	
WO_3-1%Pt	Flame spray pyrolysis	150	1000	9.9	No information	[40] (2011)
Cu-CNTs	Wet chemical	RT	50	0.018	No information	[41] (2012)
PANI/MWCNTs/SnO_2	Electrophoretic deposition/Electrochemical	RT	500	0.29	No information	[42] (2013)
B-CNTs	CVD	RT	30	0.0011	No information	[43] (2014)
TiO_2-5%WO_3 composite	Wet chemical	250	80	0.187	No information	[39] (2017)
ZnO-Nb	Thermal oxidation	425	1000	1.5	No information	[44] (2017)
β-MnO_2 nanoleaves	CVD	200	25	0.09	1.9	[31] (2018)
ZnO nanosheets	Wet chemical	500	500	3.8	5	[45] (2019)
SnO_2-Cr_2O_3	Spray pyrolysis; E-beam evaporation	350	2.5	0.168	0.024	[46] (2020)
$LaFeO_3$-1%Ag	Flame spray pyrolysis	200	50	~1.3	No information	[32] (2020)
SnO_2-Pd nanoparticles	No information	250	100	11.1	0.05	[47] (2020)
CeO_x-SnO_2	Co-precipitation	350	10	5.18	0.3	[48]

composite						(2020)
$LaFeO_3$	Sol-gel	150	500	5.5	No information	[49] (2020)
MnO_2-Au nanoneedles	CVD	150	50	0.19	0.04	[38] (2020)
MWCNTs	CVD	RT	1333	0.09	No information	[50] (2020)
ZnO-0.6Ag nanosheets	Electrodeposition	RT	50	0.0657	No information	[51] (2021)
MWCNTs	CVD	RT	10	0.28	No information	[52] (2021)
Co_3O_4-PdO_x microcages	Hydrothermal	130	50	1.8	No information	[53] (2021)
Co-Pt2 nanorods	**Hydrothermal**	**250**	**50**	**2.32**	0.13	**This work**
Co-Pt1 nanorods	**Hydrothermal**	**250**	**500**	**4.5**	-[MT1]	**This work**

The selectivity and stability of a gas sensor are crucial attributes. In Figure 13, the Co–Pt2 sensor selectivity for detecting ethylene in comparison to various other gases such as carbon monoxide, ammonia, hydrogen, ethanol, and acetone is demonstrated. The measurements were performed at a temperature of 250 °C, with each gas tested at a concentration of 100 ppm. The sensor exhibits superior selectivity for ethylene when compared to these interfering gases. This selectivity can be attributed to the binding energy and electron transfer occurring between the adsorbed molecules and the Co_3O_4 facade. These factors collectively contribute to the sensor's

effective discrimination of ethylene from other gases [54].

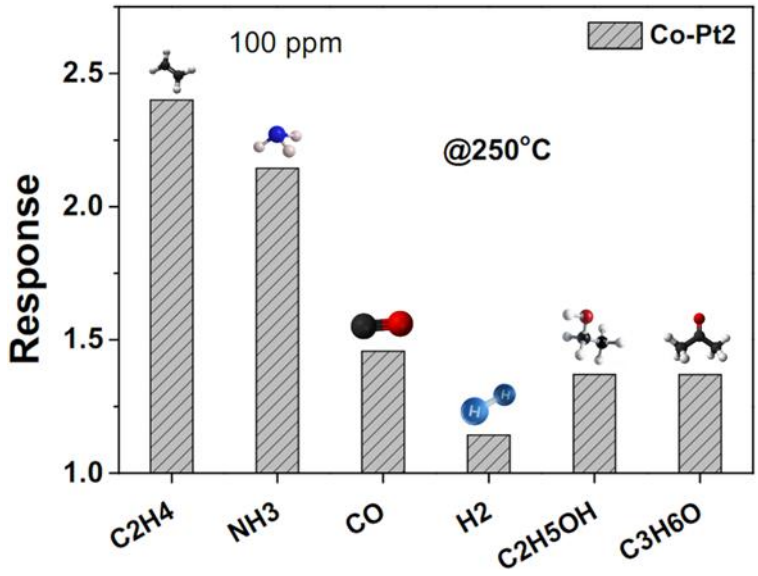

Fig. 13. Selectivity of the Co–Pt2 sensor measured at 250 °C.

Figure 14(A) presents the short-term repeatability of the Co–Pt2 sensor. The sensor exhibited good stability throughout 14 detection cycles conducted at 250 °C, with each cycle involving exposure to 500 ppm ethylene followed by return to air. Additionally, the long-term stability of the sensor was evaluated after a period of 3 months using 10 cycles identical to the previous ones, as depicted in Fig. 14(B). In both instances, the dynamic resistance demonstrated excellent stability, highlighting the suitability of the fabricated sensor for ethylene detection in fruit quality monitoring applications.

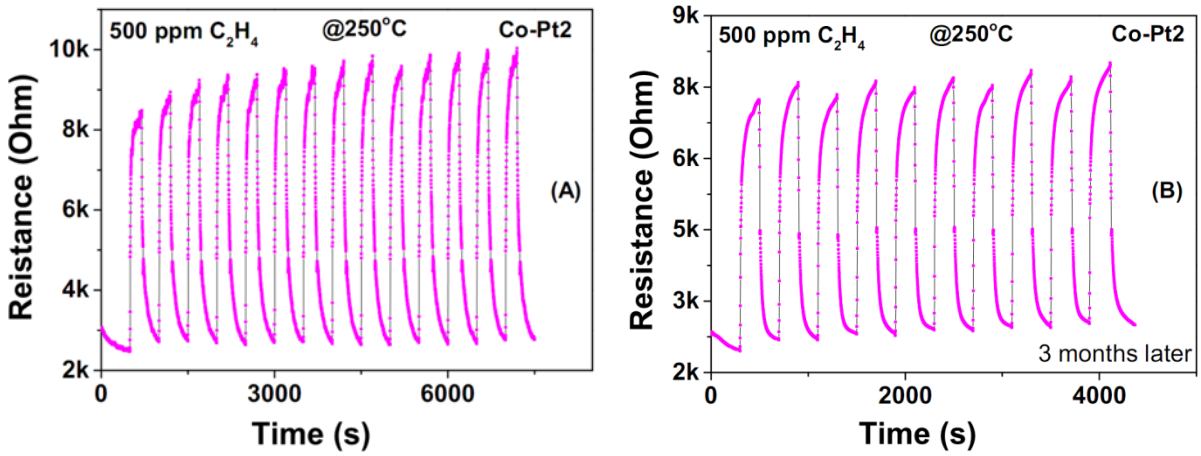

Fig. 14. (A) Stability in short-term of the Co–Pt2 sensor, and (B) after 3 months.

4. Conclusions

Porous Co_3O_4 nanorods were synthesized through a hydrothermal method followed by annealing in air and were utilized to fabricate ethylene gas sensors. To enhance the sensing performance, various quantities of Pt nanoparticles were used to functionalise the facade of the porous Co_3O_4 nanorods. Through experimentation, it was determined that a Pt amount of 0.031 wt% yielded optimal results. The Co_3O_4–Pt sensor, optimized in this manner, exhibited a response approximately 3.4 times higher than that of pure Co_3O_4. Moreover, the device demonstrated notable selectivity, outstanding short-term and long-term stability (maintained over a period of 3 months), and an ethylene detection limit of 0.13 ppm. These characteristics render the sensor well-suited for fruit quality monitoring applications.

Conflict of interest

The authors declare that there is no conflict of interest.

Acknowledgement

This research is financially funded by the Ministry of Education and Training under the research support program with the B2022-BKA-26 CTVL project.

References

[1] J. Kathirvelan, R. Vijayaraghavan, Review on sensitive and selective ethylene detection methods for fruit ripening application, Sensor Review. 40 (2020) 421–435. https://doi.org/10.1108/SR-10-2019-0251.

[2] K. Vong, S. Eda, Y. Kadota, I. Nasibullin, T. Wakatake, S. Yokoshima, K. Shirasu, K. Tanaka, An artificial metalloenzyme biosensor can detect ethylene gas in fruits and

Arabidopsis leaves, Nat Commun. 10 (2019) 5746. https://doi.org/10.1038/s41467-019-13758-2.

[3] X. Chen, R. Wreyford, N. Nasiri, Recent Advances in Ethylene Gas Detection, Materials. 15 (2022) 5813. https://doi.org/10.3390/ma15175813.

[4] S. Janssen, K. Schmitt, M. Blanke, M.L. Bauersfeld, J. Wöllenstein, W. Lang, Ethylene detection in fruit supply chains, Philosophical Transactions of the Royal Society A: Mathematical, Physical and Engineering Sciences. 372 (2014) 20130311. https://doi.org/10.1098/rsta.2013.0311.

[5] S.M. Cristescu, J. Mandon, D. Arslanov, J. De Pessemier, C. Hermans, F.J.M. Harren, Current methods for detecting ethylene in plants, Ann Bot. 111 (2013) 347–360. https://doi.org/10.1093/aob/mcs259.

[6] D.N. Son, C.M. Hung, D. Thi Thanh Le, C. Thi Xuan, N. Van Duy, N.Q. Dich, H. Nguyen, N. Van Hieu, N.D. Hoa, A novel design and fabrication of self-heated In2O3 nanowire gas sensor on glass for ethanol detection, Sens Actuators A Phys. 345 (2022) 113769. https://doi.org/10.1016/j.sna.2022.113769.

[7] M. Tonezzer, D. Thi Thanh Le, L. Van Duy, N.D. Hoa, F. Gasperi, N. Van Duy, F. Biasioli, Electronic noses based on metal oxide nanowires: A review, Nanotechnol Rev. 11 (2022) 897–925. https://doi.org/10.1515/ntrev-2022-0056.

[8] H.J. Kim, J.H. Lee, Highly sensitive and selective gas sensors using p-type oxide semiconductors: Overview, Sens Actuators B Chem. 192 (2014) 607–627. https://doi.org/10.1016/j.snb.2013.11.005.

[9] Z. Wen, L. Zhu, W. Mei, L. Hu, Y. Li, L. Sun, H. Cai, Z. Ye, Rhombus-shaped Co3O4 nanorod arrays for high-performance gas sensor, Sens Actuators B Chem. 186 (2013) 172–179. https://doi.org/10.1016/j.snb.2013.05.093.

[10] H.Y. Lee, J.H. Bang, S.M. Majhi, A. Mirzaei, K.Y. Shin, D.J. Yu, W. Oum, S. Kang, M.L. Lee, S.S. Kim, H.W. Kim, Conductometric ppb-level acetone gas sensor based on one-pot synthesized Au @Co3O4 core-shell nanoparticles, Sens Actuators B Chem. 359 (2022) 131550. https://doi.org/10.1016/j.snb.2022.131550.

[11] J. Deng, R. Zhang, L. Wang, Z. Lou, T. Zhang, Enhanced sensing performance of the Co3O4 hierarchical nanorods to NH3 gas, Sens Actuators B Chem. 209 (2015) 449–455. https://doi.org/10.1016/j.snb.2014.11.141.

[12] S. Wang, C. Xiao, P. Wang, Z. Li, B. Xiao, R. Zhao, T. Yang, M. Zhang, Co3O4 hollow nanotubes: Facile synthesis and gas sensing properties, Mater Lett. 137 (2014) 289–292. https://doi.org/10.1016/j.matlet.2014.09.021.

[13] G. Lei, C. Lou, Z. Li, J. Xie, G. Lu, H. Pan, H. Mei, X. Liu, J. Zhang, Heterogeneous Co3O4/AgO nanorods for conductometric triethylamine sensing at 90 °C, Sens Actuators B Chem. 351 (2022) 131005. https://doi.org/10.1016/j.snb.2021.131005.

[14] Y. Chen, X. Ji, Bamboo-like Co3O4 nanofiber as host materials for enhanced lithium-sulfur battery performance, J Alloys Compd. 777 (2019) 688–692. https://doi.org/10.1016/j.jallcom.2018.11.037.

[15] C. Hu, L. Yu, S. Li, M. Yin, H. Du, H. Li, Sacrificial template triggered to synthesize hollow nanosheet-assembled Co3O4 microtubes for fast triethylamine detection, Sens Actuators B Chem. 355 (2022) 131246. https://doi.org/10.1016/j.snb.2021.131246.

[16] R. Edla, N. Patel, Z. El Koura, R. Fernandes, N. Bazzanella, A. Miotello, Pulsed laser deposition of Co3O4 nanocatalysts for dye degradation and CO oxidation, Appl Surf Sci. 302 (2014) 105–108. https://doi.org/10.1016/j.apsusc.2013.10.174.

[17] S. Soltani, S.M. Rozati, M.B. Askari, Ethanol gas sensing performance of spinel Mn: Co3O4 nanostructure thin film prepared by spray pyrolysis, Micro and Nanostructures. 169 (2022) 207343. https://doi.org/10.1016/j.micrna.2022.207343.

[18] D. Barreca, D. Bekermann, E. Comini, A. Devi, R.A. Fischer, A. Gasparotto, M. Gavagnin, C. Maccato, C. Sada, G. Sberveglieri, E. Tondello, Plasma enhanced-CVD of undoped and fluorine-doped Co3O4 nanosystems for novel gas sensors, Sens Actuators B Chem. 160 (2011) 79–86. https://doi.org/10.1016/j.snb.2011.07.016.

[19] H. Nguyen, S.A. El-Safty, Meso- and Macroporous Co3O4 Nanorods for Effective VOC Gas Sensors, The Journal of Physical Chemistry C. 115 (2011) 8466–8474. https://doi.org/10.1021/jp1116189.

[20] N. Van Toan, C.M. Hung, N.D. Hoa, N. Van Duy, D. Thi Thanh Le, N. Thi Thu Hoa, N.N. Viet, P.H. Phuoc, N. Van Hieu, Enhanced NH3 and H2 gas sensing with H2S gas interference using multilayer SnO2/Pt/WO3 nanofilms, J Hazard Mater. 412 (2021) 125181. https://doi.org/10.1016/j.jhazmat.2021.125181.

[21] L.N. Minh, N.H. Loc, D.T.T. Le, M. Tonezzer, T.V.D. Ngoc, L.H. Minh, T.T.H. Duong, N.D. Hoa, Synthesis of cobalt oxide nanorods using hydrothermal method, The 5th International Conference on Advanced Materials and Nanotechnology ICAMN, November 16-19, Hanoi, Vietnam. (2022) 207–210.

[22] N.H. Hanh, L. Van Duy, C.M. Hung, C.T. Xuan, N. Van Duy, N.D. Hoa, High-performance acetone gas sensor based on Pt–Zn2SnO4 hollow octahedra for diabetic diagnosis, J Alloys Compd. 886 (2021) 161284. https://doi.org/10.1016/j.jallcom.2021.161284.

[23] F. Bonet, V. Delmas, S. Grugeon, R. Herrera Urbina, P.-Y. Silvert, K. Tekaia-Elhsissen, Synthesis of monodisperse Au, Pt, Pd, Ru and Ir nanoparticles in ethylene glycol, Nanostructured Materials. 11 (1999) 1277–1284. https://doi.org/10.1016/S0965-9773(99)00419-5.

[24] N.T. Thang, L.T. Hong, N.H. Thoan, C.M. Hung, N. Van Duy, N. Van Hieu, N.D. Hoa, Controlled synthesis of ultrathin MoS2 nanoflowers for highly enhanced NO2 sensing at

room temperature, RSC Adv. 10 (2020) 12759–12771. https://doi.org/10.1039/D0RA00121J.

[25] M. Tonezzer, T.T. Le Dang, Q.H. Tran, V.H. Nguyen, S. Iannotta, Selective hydrogen sensor for liquefied petroleum gas steam reforming fuel cell systems, Int J Hydrogen Energy. 42 (2017) 740–748. https://doi.org/10.1016/j.ijhydene.2016.11.102.

[26] D. Wang, Q. Wang, T. Wang, Morphology-controllable synthesis of cobalt oxalates and their conversion to mesoporous Co3O4 nanostructures for application in supercapacitors, Inorg Chem. 50 (2011) 6482–6492. https://doi.org/10.1021/ic200309t.

[27] B. Varghese, C.H. Teo, Y. Zhu, M. V. Reddy, B.V.R. Chowdari, A.T.S. Wee, V.B.C. Tan, C.T. Lim, C.-H. Sow, Co3O4 Nanostructures with Different Morphologies and their Field-Emission Properties, Adv Funct Mater. 17 (2007) 1932–1939. https://doi.org/10.1002/adfm.200700038.

[28] X. Wang, F. Sun, Y. Duan, Z. Yin, W. Luo, Y. Huang, J. Chen, Highly sensitive, temperature-dependent gas sensor based on hierarchical ZnO nanorod arrays, J Mater Chem C Mater. 3 (2015) 11397–11405. https://doi.org/10.1039/C5TC02187A.

[29] and K.S. Noboru Yamazoe, Go Sakai, Oxide Semiconductor Gas Sensors, Catalysis Surveys from Asia. 7 (2003) 63–75. https://doi.org/https://doi.org/10.1023/A:1023436725457.

[30] Q. Li, D. Chen, J. Miao, S. Lin, Z. Yu, D. Cui, Z. Yang, X. Chen, Highly sensitive sensor based on ordered porous ZnO nanosheets for ethanol detecting application, Sens Actuators B Chem. 326 (2021) 128952. https://doi.org/10.1016/j.snb.2020.128952.

[31] D. Barreca, A. Gasparotto, F. Gri, E. Comini, C. Maccato, Plasma-Assisted Growth of β-MnO2 Nanosystems as Gas Sensors for Safety and Food Industry Applications, Adv Mater Interfaces. 5 (2018). https://doi.org/10.1002/admi.201800792.

[32] A. Sukee, A.A. Alharbi, A. Staerz, A. Wisitsoraat, C. Liewhiran, U. Weimar, N. Barsan, Effect of AgO loading on flame-made LaFeO3 p-type semiconductor nanoparticles to acetylene sensing, Sens Actuators B Chem. 312 (2020). https://doi.org/10.1016/j.snb.2020.127990.

[33] A. Ma, S.Y. Baek, J.H. Seo, S.A. Abbas, J.-H. Kwon, S.J. Ahn, K.M. Nam, Photodeposition of Pt Nanoparticles on Co3O4 Nanocubes for Detection of Acetone at Part-Per-Billion Levels, ACS Appl Nano Mater. 4 (2021) 2752–2759. https://doi.org/10.1021/acsanm.0c03393.

[34] A. Kolmakov, D.O. Klenov, Y. Lilach, S. Stemmer, M. Moskovits, Enhanced Gas Sensing by Individual SnO2 Nanowires and Nanobelts Functionalized with Pd Catalyst Particles, Nano Lett. 5 (2005) 667–673. https://doi.org/10.1021/nl050082v.

[35] Z. Cao, W. Wang, H. Ma, L. Xiao, J. Li, Y. Sun, J. Sheng, F. Dong, Porous Mn-doped Co3O4 nanosheets: Gas sensing performance and interfacial mechanism investigation with In situ DRIFTS, Sens Actuators B Chem. 353 (2022). https://doi.org/10.1016/j.snb.2021.131155.

[36] Z. Yuan, Z. Feng, L. Kong, J. Zhan, X. Ma, Simple synthesis of porous ZnO nanoplates hyper-doped with low concentration of Pt for efficient acetone sensing, J Alloys Compd. 865 (2021). https://doi.org/10.1016/j.jallcom.2021.158890.

[37] H.Y. Lee, J.H. Bang, S.M. Majhi, A. Mirzaei, K.Y. Shin, D.J. Yu, W. Oum, S. Kang, M.L. Lee, S.S. Kim, H.W. Kim, Conductometric ppb-level acetone gas sensor based on one-pot synthesized Au @Co3O4 core-shell nanoparticles, Sens Actuators B Chem. 359 (2022). https://doi.org/10.1016/j.snb.2022.131550.

[38] L. Bigiani, D. Zappa, E. Comini, C. Maccato, A. Gasparotto, D. Barreca, Manganese Oxide Nanoarchitectures as Chemoresistive Gas Sensors to Monitor Fruit Ripening, J Nanosci Nanotechnol. 20 (2019) 3025–3030. https://doi.org/10.1166/jnn.2020.17479.

[39] J. Kathirvelan, R. Vijayaraghavan, A. Thomas, Ethylene detection using TiO2-WO3 composite sensor for fruit ripening applications, Sensor Review. 37 (2017) 147–154. https://doi.org/10.1108/SR-12-2016-0262.

[40] T. Samerjai, N. Tamaekong, C. Liewhiran, A. Wisitsoraat, A. Tuantranont, S. Phanichphant, Selectivity towards H2 gas by flame-made Pt-loaded WO 3 sensing films, Sens Actuators B Chem. 157 (2011) 290–297. https://doi.org/10.1016/j.snb.2011.03.065.

[41] B. Esser, J.M. Schnorr, T.M. Swager, Selective detection of ethylene gas using carbon nanotube-based devices: Utility in determination of fruit ripeness, Angewandte Chemie - International Edition. 51 (2012) 5752–5756. https://doi.org/10.1002/anie.201201042.

[42] P. Pattananuwat, D. Aht-Ong, In-Situ Electrochemical Synthesis of Novel Sensitive Layer of Polyaniline/Multiwall Carbon Nanotube/Tin Oxide Hybrid Materials for Ethylene Gas Detection, Polymer - Plastics Technology and Engineering. 52 (2013) 189–194. https://doi.org/10.1080/03602559.2012.735312.

[43] J.-J. Adjizian, R. Leghrib, A.A. Koos, I. Suarez-Martinez, A. Crossley, P. Wagner, N. Grobert, E. Llobet, C.P. Ewels, Boron- and nitrogen-doped multi-wall carbon nanotubes for gas detection, Carbon N Y. 66 (2014) 662–673. https://doi.org/10.1016/j.carbon.2013.09.064.

[44] E. Wongrat, N. Chanlek, C. Chueaiarrom, W. Thupthimchun, B. Samransuksamer, S. Choopun, Acetone gas sensors based on ZnO nanostructures decorated with Pt and Nb, Ceram Int. 43 (2017) S557–S566. https://doi.org/10.1016/j.ceramint.2017.05.296.

[45] L.P. Wang, Z. Jin, T. Luo, Y. Ding, J.H. Liu, X.F. Wang, M.Q. Li, The detection of ethylene using porous ZnO nanosheets: utility in the determination of fruit ripeness, New Journal of Chemistry. 43 (2019) 3619–3624. https://doi.org/10.1039/c9nj00031c.

[46] S.Y. Jeong, Y.K. Moon, T.H. Kim, S.W. Park, K.B. Kim, Y.C. Kang, J.H. Lee, A New Strategy for Detecting Plant Hormone Ethylene Using Oxide Semiconductor Chemiresistors: Exceptional Gas Selectivity and Response Tailored by Nanoscale Cr2O3 Catalytic Overlayer, Advanced Science. 7 (2020) 1–11. https://doi.org/10.1002/advs.201903093.

[47] Q. Zhao, Z. Duan, Z. Yuan, X. Li, W. Si, B. Liu, Y. Zhang, Y. Jiang, H. Tai, High performance ethylene sensor based on palladium-loaded tin oxide: Application in fruit quality detection, Chinese Chemical Letters. 31 (2020) 2045–2049. https://doi.org/10.1016/j.cclet.2020.04.032.

[48] P. Leangtanom, A. Wisitsoraat, K. Jaruwongrungsee, N. Chanlek, S. Phanichphant, V. Kruefu, Highly sensitive and selective ethylene gas sensors based on CeOx-SnO2 nanocomposites prepared by a Co-precipitation method, Mater Chem Phys. 254 (2020) 123540. https://doi.org/10.1016/j.matchemphys.2020.123540.

[49] A.A. Alharbi, A. Sackmann, U. Weimar, N. Bârsan, A highly selective sensor to acetylene and ethylene based on LaFeO3, Sens Actuators B Chem. 303 (2020) 127204. https://doi.org/10.1016/j.snb.2019.127204.

[50] N.M. Shaalan, F. Ahmed, S. Kumar, A. Melaibari, P.M.Z. Hasan, A. Aljaafari, Monitoring Food Spoilage Based on a Defect-Induced Multiwall Carbon Nanotube Sensor at Room Temperature: Preventing Food Waste, ACS Omega. 5 (2020) 30531–30537. https://doi.org/10.1021/acsomega.0c04396.

[51] A. Sholehah, K. Karmala, N. Huda, L. Utari, N.L.W. Septiani, B. Yuliarto, Structural effect of ZnO-Ag chemoresistive sensor on flexible substrate for ethylene gas detection, Sens Actuators A Phys. 331 (2021) 112934. https://doi.org/10.1016/j.sna.2021.112934.

[52] N.M. Shaalan, O. Saber, F. Ahmed, A. Aljaafari, S. Kumar, Growth of defect-induced carbon nanotubes for low-temperature fruit monitoring sensor, Chemosensors. 9 (2021) 16–19. https://doi.org/10.3390/chemosensors9060131.

[53] W. Wang, W. Jin, S. Yang, Z. Jian, W. Chen, PdOx decorated Co3O4 nanosheets-assembled hollow microcages for enhanced ethanol sensing performance, Sens Actuators B Chem. 333 (2021). https://doi.org/10.1016/j.snb.2021.129583.

[54] N.H. Hanh, L. Van Duy, C.M. Hung, C.T. Xuan, N. Van Duy, N.D. Hoa, High-performance acetone gas sensor based on Pt–Zn2SnO4 hollow octahedra for diabetic diagnosis, J Alloys Compd. 886 (2021) 161284. https://doi.org/10.1016/j.jallcom.2021.161284.